nature materials

ARTICLES

PUBLISHED ONLINE: 5 FEBRUARY 2012 | DOI: 10.1038/NMAT3238

Self-limited plasmonic welding of silver nanowire junctions

Erik C. Garnett[1], Wenshan Cai[1], Judy J. Cha[1], Fakhruddin Mahmood[1,2], Stephen T. Connor[1], M. Greyson Christoforo[1], Yi Cui[1,3], Michael D. McGehee[1] and Mark L. Brongersma[1]*

Nanoscience provides many strategies to construct high-performance materials and devices, including solar cells, thermoelectrics, sensors, transistors, and transparent electrodes. Bottom-up fabrication facilitates large-scale chemical synthesis without the need for patterning and etching processes that waste material and create surface defects. However, assembly and contacting procedures still require further development. Here, we demonstrate a light-induced plasmonic nanowelding technique to assemble metallic nanowires into large interconnected networks. The small gaps that form naturally at nanowire junctions enable effective light concentration and heating at the point where the wires need to be joined together. The extreme sensitivity of the heating efficiency on the junction geometry causes the welding process to self-limit when a physical connection between the wires is made. The localized nature of the heating prevents damage to low-thermal-budget substrates such as plastics and polymer solar cells. This work opens new avenues to control light, heat and mass transport at the nanoscale.

Light-induced heating of materials is a well known phenomenon and has been implemented in applications ranging from rapid thermal annealing to solar thermal energy conversion. At the most basic level, light-induced heat generation depends only on two factors: material absorption and light intensity. As metals exhibit large Ohmic losses and enable effective light concentration, they serve as efficient, light-driven sources of heat[1,2]. With the use of pulsed lasers one has the ability to rapidly raise and lower the temperature in nanoscale metallic structures and to thermally stimulate a wide range of physical processes and chemical reactions with unprecedented spatial and temporal control[2]. This has already resulted in applications such as selective identification and killing of cancer cells[3], modification of polymer surfaces[4], local control over phase transitions[5,6], growth of individual semiconductor nanowires and carbon nanotubes[7], nanofluidics and chemical separation[8] and reversible photothermal melting of DNA (ref. 9). In many of these applications, the ability to heat only locally rather than globally has resulted in major increases in control, speed and energy efficiency with an accompanying reduction in cost.

In this work, we explore and use the effects of local heat generation in closely spaced metallic nanostructures that exhibit a strong optical interaction. The science of optically coupled metallic nanostructures is at present receiving significant attention[10] and such structures are increasingly used in a wide variety of applications, including surface-enhanced Raman scattering (SERS) with single-molecule sensitivity[11], nanoscale optical waveguides[12] and metamaterials exhibiting a negative index[13,14] or intriguing polarization properties[15]. Particularly rich and exciting physics comes into play when metallic particles are brought into such close proximity that charge-transfer, non-local and quantum mechanical effects become important[16–18]. These distances can now be experimentally controlled[19] and may soon become commonplace in plasmonic devices. In this work, we take advantage of the large field enhancement that can occur in the nanoscale gap between two crossed silver nanowires to weld them together in a highly controlled and self-limiting fashion.

Our fundamental study has immediate technological applications for large-scale metallic nanowire mesh films, which have received increasing attention recently as a potential high-throughput, low-cost, solution-processable replacement for the transparent conductive oxides used in touch-screens, displays, light-emitting diodes and thin-film solar cells[20–29]. One challenge in implementing metallic nanowires is that the insulating ligands used for the synthesis and solution dispersion need to be removed after deposition to ensure high wire–wire junction conductivity. This is usually done through heating or mechanical pressing, both of which can damage delicate devices such as organic solar cells. Here, we show that our plasmonic welding technique provides extreme heating locally at the junctions without substantially affecting the surrounding materials. This enables us to make high-performance, welded silver nanowire mesh electrodes on top of heat-sensitive materials and devices, such as plastic wrap and polymer solar cells.

Figure 1a shows a schematic of our experimental set-up and illustrates the nanowelding procedure. Pentagonally twinned silver nanowires were synthesized by the polyol process, leading to a distribution of diameters between 30 and 80 nm and lengths between 3 and 10 μm, with the surfaces capped by polyvinylpyrrolidone (PVP; ref. 30). They were dropcast onto suspended silicon nitride membranes to form nanowire junctions and exposed to a broadband tungsten–halogen lamp at a power density of approximately 30 W cm^{-2} for 10–120 s. The nanowire junctions were characterized before and after illumination by means of scanning electron microscopy (SEM), transmission electron microscopy (TEM), dark-field confocal spectroscopy, optical transmission and electrical resistance measurements. Figure 1b,c show plan view SEM images collected before and after 60 s

[1]Geballe Laboratory for Advanced Materials, Stanford University, Stanford, California 94305-4045, USA, [2]Department of Electrical Engineering, King Abdullah University of Science and Technology, Thuwal 23955-6900, Saudi Arabia, [3]Stanford Institute for Materials and Energy Sciences, SLAC National Accelerator Laboratory, Menlo Park, California 94025-7015, USA. *e-mail: brongersma@stanford.edu.

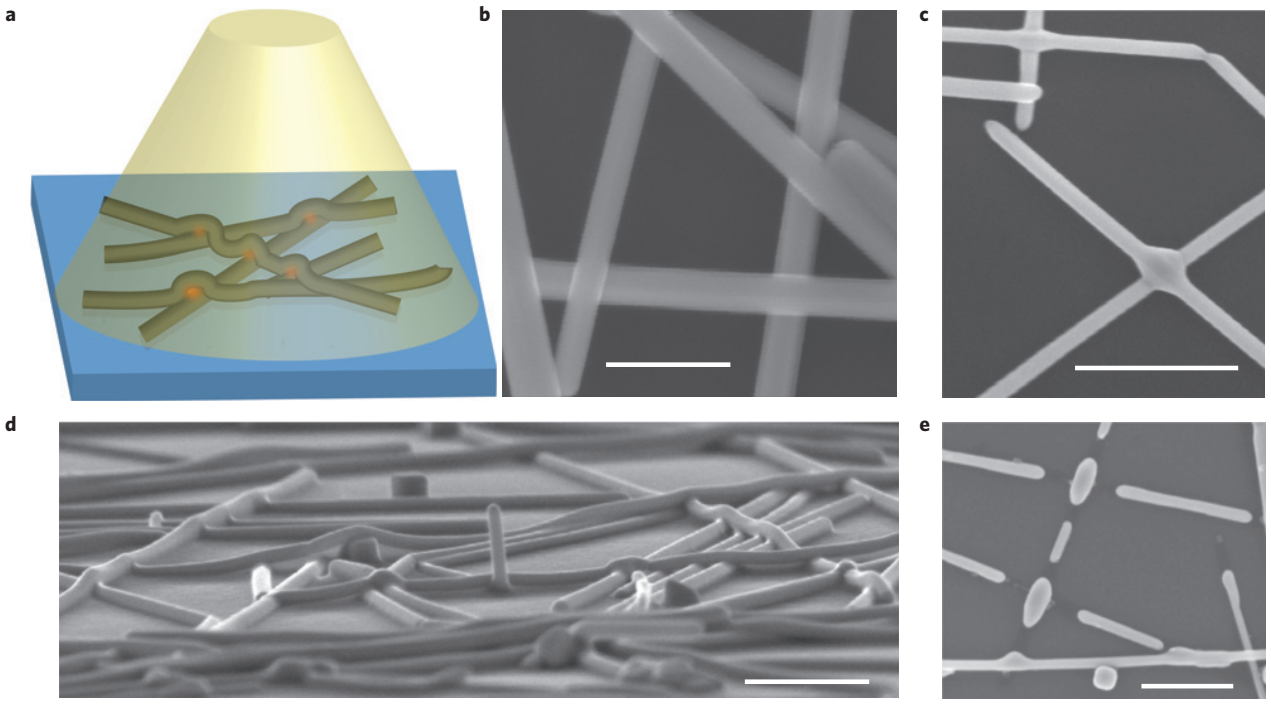

Figure 1 | Optical nanowelding set-up and scanning electron microscope (SEM) images before and after illumination. a, Schematic of the illumination geometry for silver nanowire junction plasmonic welding on a suspended silicon nitride membrane (blue) with a silicon wafer for structural support (not shown). The wire junctions naturally feature nanometre-scale gaps due to the presence of surface ligands on the wires. These small gaps enable extreme local heating due to the strong field concentration (red). **b**, Plan-view SEM image of silver nanowire junctions before illumination. Scale bar is 200 nm. **c**, Plan-view SEM image of silver nanowire junctions after optical welding with a tungsten halogen lamp. Scale bar is 500 nm. **d**, Tilted cross-sectional SEM image of the sample shown in **c**. Scale bar is 500 nm. **e**, Plan-view SEM image of silver nanowire junctions after uniform heating on a hotplate. Heating times between 15–60 s and 200–300 °C either showed no visible change (looked like **b**) or broken junction points, as shown here. This lack of control with uniform heating underscores the importance of the self-limited optical nanowelding process. Scale bar is 500 nm.

of illumination with the lamp. Before illumination, individual nanowires were clearly distinct throughout the junctions but afterwards the morphology changed substantially and the junctions were welded together. Importantly, away from each junction the nanowires were unaffected by the illumination and no further morphological changes were observed on prolonged illumination (Supplementary Fig. S1). Tilted cross-sectional SEM images were taken after illumination to further elucidate the materials science governing the welding process (Fig. 1d). The optically nanowelded junctions showed a distinctly different morphology from those heated uniformly by a hotplate. Whereas the optical nanowelding process self-limits, the thermal treatment with a hot plate either showed no melting or an undesired breaking up of the nanowires (Fig. 1e) consistent with a Rayleigh instability[31]. This difference underscores the strength of the optical nanowelding process, which allows junctions in the nanowire network to be welded and electrically connected without breaking up the wires.

Figure 2 shows TEM images of representative junctions before and after illumination. In the as-made samples, each nanowire showed dark bands running along its length originating from the pentagonally twinned nanowire crystal structure[32]. The continuous nature of these bands along the length of each nanowire indicates that there are two different crystal orientations (one for each nanowire) at the junction point (Fig. 2a). However, after illumination the dark bands were interrupted at the junction for the bottom nanowire but continued undisturbed through the junction in the top nanowire (Fig. 2b,c). This suggests that there is only one crystal orientation at the junction point and it matches that of the top nanowire. During the optical welding process, the atoms in the bottom wire must have exhibited significant mobility, allowing epitaxial recrystallization onto the top wire locally at the junction. The top and bottom nanowires were differentiated by the junction asymmetry observed in the SEM images after nanowelding and confirmed by tilted SEM imaging.

Further evidence of this epitaxial recrystallization comes from the selected area electron diffraction (SAED) patterns collected for representative junctions before and after the nanowelding process (Fig. 3a–d and e,f, respectively). Before illumination, SAED patterns from each nanowire were consistent with previous reports of pentagonally twinned silver nanowires sitting on the substrate with one of the five equivalent crystal facets lying flat[32]. The pentagonally twinned crystals gave rise to relatively weak double diffraction spots in between the stronger primary spots along only one direction, leading to parallel lines of spots (Fig. 3b,c; the blue and red lines, respectively, run parallel to the diffraction spots arising from twinning and are guides for the eye). At the junction, the double diffraction spots were visible along two directions, with roughly equal intensity and rotated by approximately ninety degrees, leading to a grid pattern (Fig. 3d). However, after illumination the junction showed double diffraction spots primarily along a single direction, matching the pattern from the top nanowire away from the junction (Fig. 3f,b, respectively). The few faint spots associated with the bottom nanowire SAED pattern appear because the smallest diffraction aperture available was slightly larger than the nanowelded junction and the bottom nanowire maintained its original crystal orientation outside of the junction region. Lattice-resolved TEM images taken at the junction and on each individual nanowire confirmed that only one crystal orientation existed at the junction and it was the same as that of the top nanowire (Fig. 2d and Supplementary Fig. S2). This suggests that at the crossing point, the epitaxial recrystallization does not occur exclusively at the interface between the nanowires, but completely throughout the

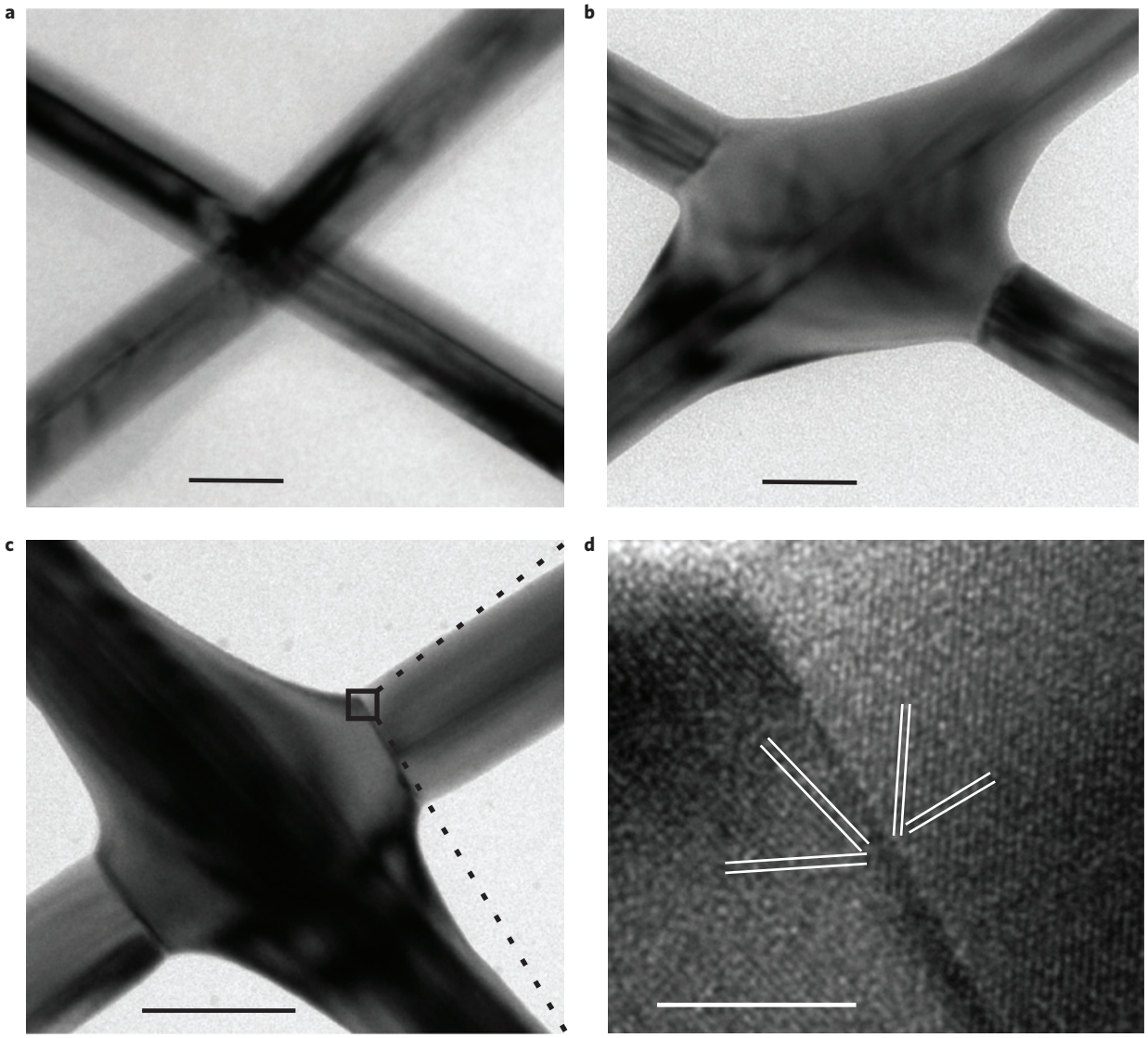

Figure 2 | Transmission electron microscope (TEM) images before and after illumination. a, TEM image of an as-made silver nanowire junction. Evidence of twinning planes running along the length of each nanowire is visible throughout the junction in both directions. Scale bar is 50 nm. **b**,**c**, TEM images of silver nanowire junctions after optical welding. In every melted junction the twinning planes stopped abruptly in the bottom nanowire and only continued through the junction for the top nanowire, indicating the bottom nanowire recrystallized epitaxially onto the top nanowire. The bottom and top nanowires were differentiated by the junction asymmetry identified in Fig. 1c and confirmed by tilted SEM imaging. Scale bars are 50 nm. **d**, Lattice-resolved TEM image of the interface between the bottom nanowire and the junction, showing an abrupt change in crystal orientation. Scale bar is 5 nm.

bottom nanowire. Away from the junction the bottom nanowire maintained its original crystal orientation, leading to distinct grain boundaries on each side of the junction.

Epitaxial recrystallization, a specific type of secondary (or abnormal) grain growth, has been observed and studied extensively in thin films[33]. Normal grain growth terminates when the average grain size approaches the film thickness; beyond that point secondary growth can enlarge certain grains at the expense of others. A lattice-matched substrate can help drive epitaxial recrystallization due to the gain in interfacial free energy, although this depends on factors such as temperature, pressure, surface morphology, self-diffusivity and chemical environment. Whereas in semiconductors grain growth requires temperatures approaching the melting point (T_{mp}), in metals it can occur at temperatures as low as $0.2T_{mp}$ (ref. 33). For many metals, including silver, this means that grain growth can occur near room temperature and, indeed, cold welding has been observed in ultrathin gold nanowires under ultra-high vacuum[34]. Although there have been numerous reports of nanoparticle, nanowire and nanotube welding, all of them either had a morphology change in the entire structure (including away from the junction) or showed only a surface atom reorganization[35–42]. Here, we provide the first evidence for complete epitaxial recrystallization that is spatially limited to the nanowire junctions, where the top nanowire acts as a nucleation template to locally reorient the bottom nanowire. This heating and recrystallization behaviour is highly localized, as a single nanowire can both act as a nucleation template at one junction and reorient at another within the space of only approximately 1 μm (Supplementary Fig. S3). Although we have not measured the junction temperature during the optical nanowelding process, we know it must exceed 150 °C because even extended heating (>20 min) at that temperature does not substantially affect the junction morphology. At that temperature, silver atom self-diffusion at grain boundaries is fast enough to allow junction recrystallization in less than one second[43]. This indicates that PVP removal may be the rate-determining step, underscoring

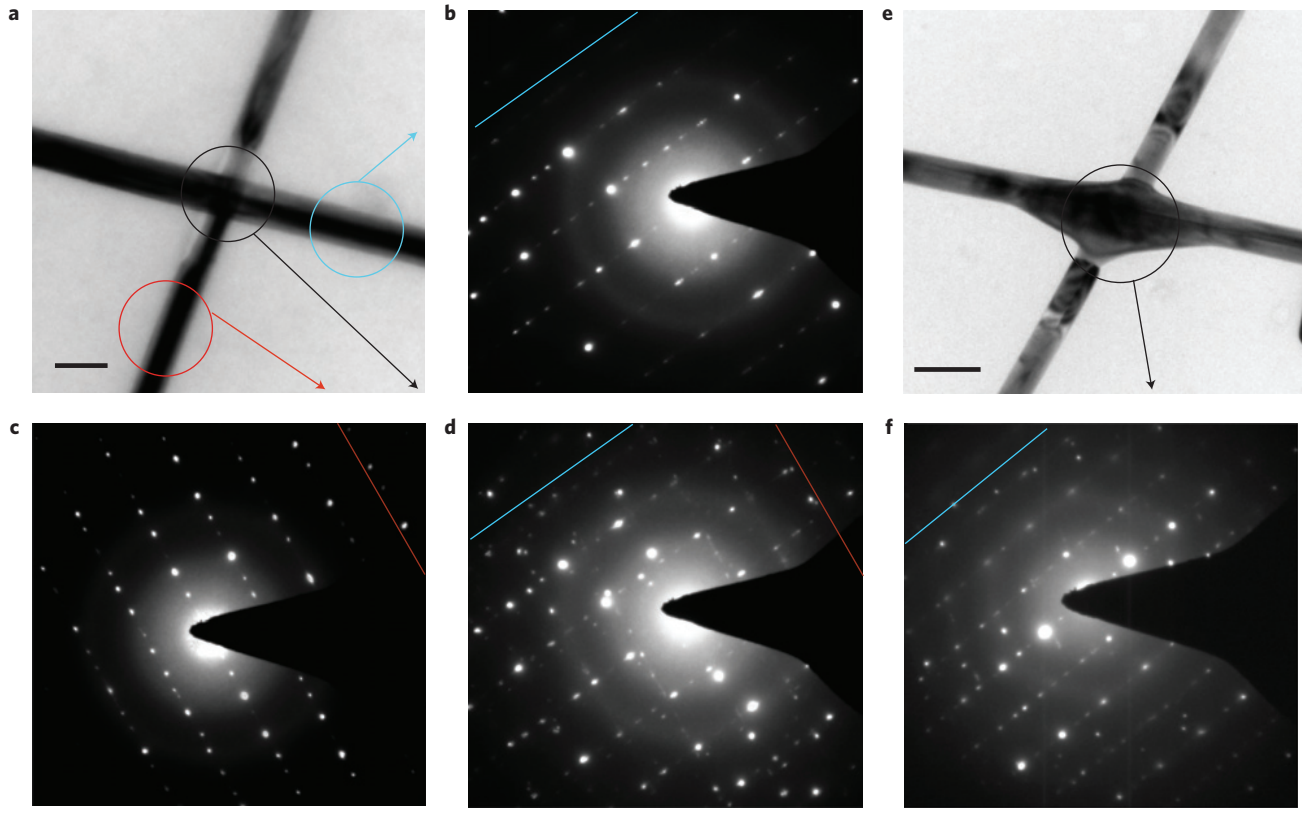

Figure 3 | Selected area electron diffraction (SAED) of silver nanowire junctions before and after illumination. a, Low-magnification TEM image of a silver nanowire junction before illumination. The circles represent the approximate size and location of the diffraction apertures used for the SAED patterns in **b**–**d**. Scale bar is 100 nm. **b**, SAED pattern of the top nanowire away from the junction. The large number of double diffractions caused by the pentagonally twinned cross-section lead to prominent lines of spots in only one direction, parallel to the blue line. **c**, SAED pattern of the bottom nanowire away from the junction. The double diffraction spots occur in a direction roughly perpendicular to that in **b** and parallel to the red line. **d**, SAED pattern of the junction. Both sets of spots from **b** and **c** are visible. The double diffraction spots create a grid instead of an array of parallel lines as in **b** and **c**. **e**, Low-magnification TEM image of a silver nanowire junction after illumination and nanowelding. The circle represents the approximate size and location of the diffraction aperture used for the SAED pattern in **f**. Scale bar is 100 nm. **f**, SAED pattern of the junction showing primary contributions from the crystal orientation of the top nanowire (as in **b**, lines of spots parallel to the blue line).

the importance of our self-limited plasmonic heating process in reaching the final welded state for most junctions in the film.

To understand the self-limiting nature of the nanowelding process, we performed finite element method (FEM) electromagnetic simulations on silver nanowire junctions. In the simulations, we considered a plane wave illumination of two silver nanowires crossed at ninety degrees, suspended in air, and separated by 2 nm, which is an estimate for the ligand spacing caused by the surface PVP. Without loss of the essential physics, each nanowire was modelled as having a circular cross-section and a 100 nm diameter. The simulations provided local electric field values and the local heat generation (that is, light absorption) was determined from the electric field squared times the imaginary part of the dielectric function[1]. Figure 4a–c repectively shows cross-sectional views of the heat generation profiles for junctions with a 2 nm gap and for touching/interpenetrating wires exhibiting a 2 nm overlap and a 50 nm overlap. With these simulations we aim to capture the basic progression in the morphological states during the welding process from initially separated wires to the final welded state. Before illumination (2 nm gap), the heat generation primarily occurs in the bottom nanowire at the junction point. This is consistent with the experiments where the bottom nanowires recrystallized epitaxially onto the top nanowires (Figs 2, 3; Supplementary Fig. S3). As soon as the nanowires begin to weld together (-2 nm gap $= 2$ nm overlap) the heat generation moves away from the original junction point to the seam between the nanowires. This creates a 'zipper' effect, where the heat generation is always peaked at the edge of the gap and moves outwards. As the welding process progresses, the heat generation rapidly drops off (Fig. 4c). Figure 4d plots the heat generation efficiency, defined as the fraction of incident light power that is converted to heat (calculated for a 100 nm section of each nanowire around the junction) as a function of gap size for gaps between 500 nm and -100 nm (100 nm overlap). It shows that as the nanowires come closer together, the field concentration effect increases and the heat generation spikes. Once the wires touch, the heating rapidly becomes less effective and the wire cools. This property explains the self-limiting aspect of optical nanowelding.

To further explore the nature of the heating process, we also performed spectrally and polarization dependent simulations of the heat generation efficiency. Figure 4e shows the wavelength dependence of the heat generation efficiency in a silver nanowire junction with a 2 nm gap. When the electric field is directed normal to the top wire axis (red curve and schematic) a strong, broad peak around 450 nm is observed. For the orthogonal polarization (blue curve and schematic), the heat generation is significantly reduced. This indicates that even greater control over individual junction heating may be possible by using a narrow-band, polarized source with a wavelength around 450 nm. However, because the field concentration depends sensitively on the gap, crossing angle and nanowire diameter, a broadband source such as we have demonstrated will probably be better for large-area applications that require welding many different junctions.

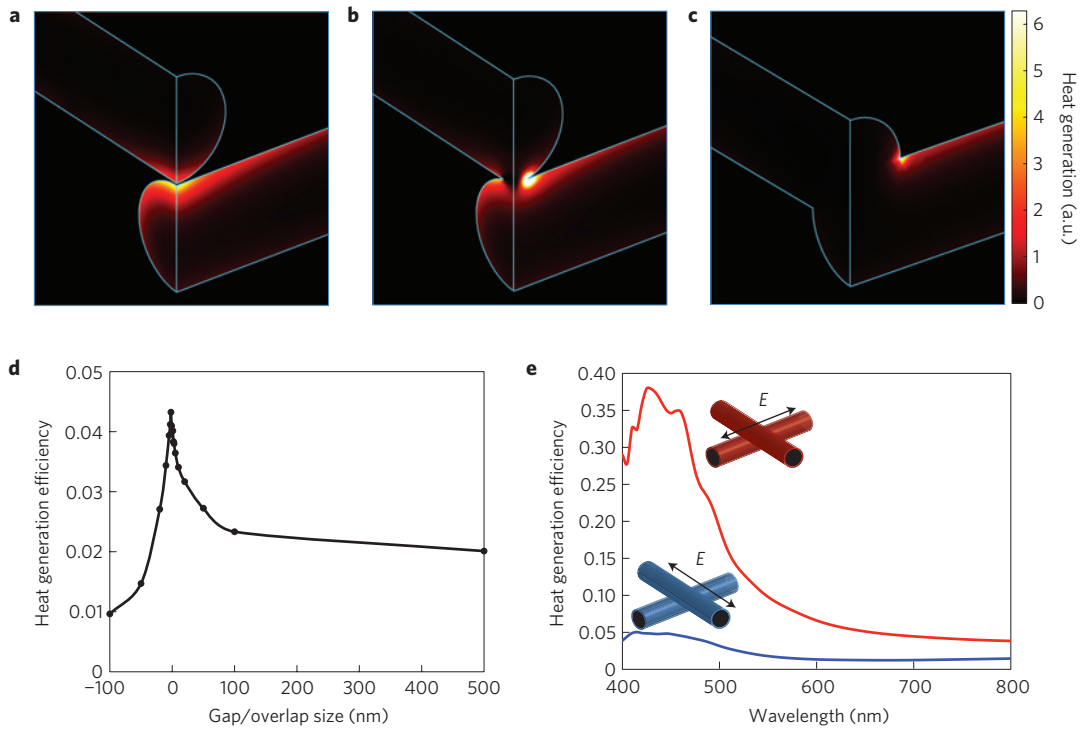

Figure 4 | Finite element method simulations of optical heat generation at silver nanowire junctions during the nanowelding process. a, Cross-sectional view of the heat generation profile for a junction with a 2 nm gap between silver nanowires with a 100 nm diameter and circular cross-section. The thin blue lines define the edges of the nanowire for clarity. The illumination source is a plane wave with a wavelength of 800 nm, incident from the top and polarized perpendicular to the top nanowire. The surrounding environment is air. Heat generation occurs primarily in the bottom nanowire within a few nanometres of the gap. **b**, Cross-sectional view of the heat generation profile in a junction immediately after epitaxial recrystallization begins. The simulation geometry is exactly the same as in **a**, except that now the nanowires are assumed to be interpenetrating with a 2 nm overlap. The heat generation has moved along the seam formed by the nanowelding process. **c**, Cross-sectional view of the heat generation profile in a junction after complete epitaxial recrystallization, with an overlap between the cylinders of 50 nm. **d**, Total heat generation efficiency integrated over a 100 nm section around each junction versus gap/overlap size. Negative values on the *x* axis correspond to interpenetrating nanowires (after epitaxial recrystallization). **e**, Heat generation efficiency as a function of wavelength for light polarized perpendicular (red) or parallel (blue) to the top nanowire for a junction with a 2 nm gap.

The observations that the local heating strongly depends on the inter-wire spacing as well as the illumination wavelength and polarization provide evidence for the importance of plasmon excitations in the nanowelding process. From Fig. 4e it is clear that heating is most efficient when the illumination wavelength is close to the localized surface plasmon (LSP) resonance of an individual silver nanowire and when the polarization direction is correct to effectively drive such a resonance in the top nanowire, as determined by polarization selection rules. From extensive work on coupled systems of nanowires[44], nanoparticles and films[45–48], as well as nanowires and nanoparticles[49–52], it is well established that high localized fields, known as 'hot spots', can be generated in the junctions of these systems. In this work, these hot spots in the optical field are used to generate real hot spots in thermal distribution near the junction. By exploiting such thermal hot spots, the wires can be welded together without generating significant heat in the rest of the wires or the underlying material. Previous work has convincingly shown that the top nanowire can serve as an efficient nanoscale antenna capable of directing light into the bottom wire[49]. This antenna action is derived from the effective electromagnetic coupling between the LSP that can be driven in the top wire and the plasmons in the bottom nanowire. This effective 'focusing' of light by the top wire into the bottom wire results in the observed preferential heating of the bottom wire (consistent with Fig. 4a). When the light is polarized along the top nanowire, a LSP cannot be excited in this wire and instead the light is strongly backscattered, reducing field penetration into the junction and leading to less heat generation. These observations are consistent with far-field light scattering measurements under bright-field and dark-field illumination (Supplementary Fig. S4). As soon as the wires are physically welded together, the gap plasmon modes in the wire junction can no longer be excited and the heat generation is significantly reduced. This physically explains why the optical nanowelding process self-limits.

It is expected that the marked change in the local near-field optical interaction on welding produces a concomitant change in the far-field light scattering. To test this, we used a confocal microscope to measure the dark-field scattering spectra[53] of nanowire junctions before and after optical nanowelding. Figure 5 shows a typical example. Before illumination, the peak in the junction scattering spectrum was similar to previous reports on individual silver nanowires[54]. After illumination and nanowelding, the main peak red-shifted, broadened and increased in intensity. These general spectral changes were observed for a number of junctions, although the exact spectral shapes varied. This is consistent with the fact that LSPs are very sensitive to the geometry, shape and size of the building blocks. In general, larger and more complex metallic systems exhibit the type of spectral broadening and red-shifts seen in this experiment. Interestingly, the scattering spectrum began to change after 30 s of illumination, but a morphology change at the junction was visible (as in Supplementary Figs S1–S3) only after 60 s. Prolonged illumination showed no substantial change in the welded morphology (Supplementary Fig. S1) and scattered light intensity, although a noticeable change in the spectral scattering properties was observed (Fig. 5a). These results suggest that dark-field scattering can serve as a very sensitive

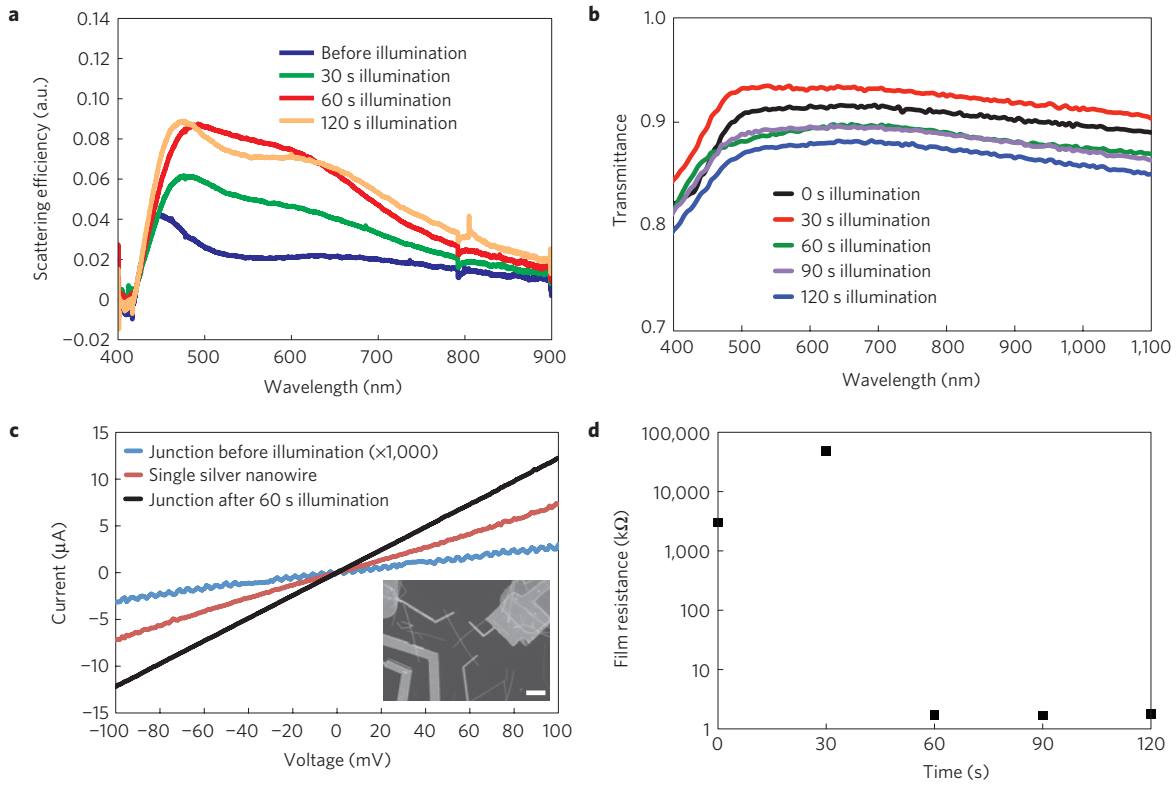

Figure 5 | Optical and electrical properties of silver nanowire junctions before and after illumination. a, Dark-field scattering spectrum of a single silver nanowire junction before (blue), after 30 s (green), after 60 s (red), and after 120 s (orange) of illumination with a tungsten halogen lamp. There was no apparent change in the SEM image after 30 s illumination, but after 60 s the junction welded together (Figs 1–3). The red-shift, broadening, and increased intensity in the scattering peak caused by the nanowelding process appeared even before any structural changes were visible in the SEM, indicating that the localized plasmon resonance is very sensitive to changes in the junction morphology. **b**, Optical transmittance of a silver nanowire mesh transparent electrode versus wavelength and illumination time. The plot shows the total transmittance as a function of wavelength for different welding times. An integrating sphere was used to ensure that all transmitted light (including high-angle scattering) was collected. The small differences in overall transmission arise from variations in nanowire density from sample to sample. The junction area only covers approximately 1% of the total area and therefore is not expected to have pronounced effects on the macroscopic optical properties of the mesh. **c**, Individual silver nanowire and junction resistance. The plot shows current–voltage traces for a single silver nanowire and a crossed nanowire junction before and after 60 s illumination. The current values for the pre-illuminated junction were multiplied by 1,000 to put it on the same scale as the other traces, demonstrating that the junction resistance drops by more than three orders of magnitude after illumination and welding. The welded junction shows a comparable resistance to the single nanowire, indicating excellent electrical contact. The inset shows a SEM image of a single nanowire device. Scale bar is 2 μm. **d**, Silver nanowire mesh transparent electrode resistance versus illumination time. The plot shows the four-point probe resistance as a function of illumination time for silver nanowire networks with an area of ~5 cm^2. The resistance is initially very high and after 30 s does not decrease, but after 60 s it drops by more than three orders of magnitude, consistent with single junction resistance measurements. Further illumination does not change the film resistance, demonstrating the self-limited nature of the plasmonic welding process.

probe of the plasmonic coupling at the junction and provides an elegant and rapid method for tracking the welding process without the need for high-resolution electron microscopy techniques.

To demonstrate the practicality of our nanoscale welding process in macroscale applications, we have fabricated and tested transparent electrodes consisting of large-area (~5 cm^2) silver nanowire meshes made by spray-coating. Typical meshes made this way have average nanowire spacings of approximately 1 μm. To track the self-limited nature of the optical welding, we monitored the four-point electrode resistance as a function of illumination time for transparent electrodes with relatively low but uniform nanowire densities, where the junction resistance is expected to be especially important. The electrode resistance remains high after a 30 s illumination, but drops by a factor of over a thousand after 60 s and then plateaus to 120 s (Fig. 5d). This large drop in resistance is consistent with the resistance drops seen on welding junctions of crossed single nanowires (Fig. 5c). Before illumination, the junction resistance is roughly three orders of magnitude higher than the single nanowire resistance, but after optical welding they are comparable. This demonstrates that the electrode resistance is initially dominated by individual junctions, but after welding also has major contributions from the nanowires themselves. The wavelength-dependent transmission of the silver nanowire electrodes is almost the same before and after welding, with minor increases or decreases related to variations in the nanowire density (Fig. 5b). The slight change in shape after 60 s of illumination in the 400–500 nm region is consistent with the reduced heating after welding. This effect is subtle, as the junction area only represents approximately 1% of the electrode area. A silver nanowire transparent electrode with a more optimal density for commercial applications formed by plasmonic welding has a four-point resistance of 10 Ω and transmittance of approximately 80% across the entire spectral region measured (Supplementary Fig. S5).

To further demonstrate the localized nature of the heating, we produced spray-coated and plasmonically welded silver nanowire mesh electrodes on top of plastic wrap (Saran wrap, made from low-density polyethylene) and polymer bulk heterojunction solar cells. Once again, 60 s of illumination reduced the sheet

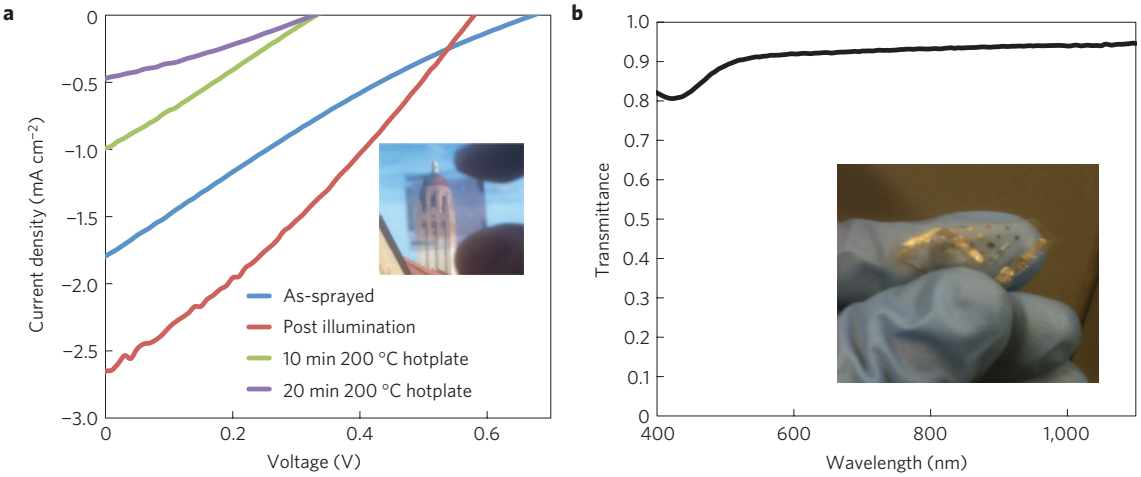

Figure 6 | Applications of local plasmonic heating on temperature-sensitive materials and devices. a, Current density–voltage curves of semitransparent polymer solar cells made with spray-coated silver nanowire top electrodes. The as-sprayed performance (blue curve) improves by a factor of two after plasmonic welding (red curve) but degrades substantially after 10 min of heating at 200 °C on a hotplate (green curve) and by an order of magnitude after 20 min of heating (violet curve). The inset is a picture of Hoover Tower on the Stanford University campus seen through the semitransparent solar cell. This type of cell could be used as a window tinting that also generates electrical power. **b**, Transparent electrodes made by spray-coating silver nanowires on plastic wrap (Saran wrap made from low-density polyethylene) followed by plasmonic welding. The transmittance reaches up to 95% for a sheet resistance as low as 580 Ω per square. The inset is a picture of the film being bent in half. The gold and silver coloured regions are evaporated metal pads used to define contacts for 2- and 4-point resistance measurements. The Supplementary Information shows a video demonstrating the extreme durability of these electrodes (Supplementary Information S6).

resistance by more than three orders of magnitude and improved the polymer solar cell efficiency by a factor of two over the as-sprayed films and an order of magnitude over the standard hotplate treatment (Fig. 6). The standard hotplate treatment could not be used for the silver nanowire electrodes on Saran wrap as the film began to melt at approximately 150 °C. The silver nanowire films on Saran wrap are extremely durable, withstanding folding, bending and even crumpling without significant changes in resistance (Supplementary Video S6). The ultimate power conversion efficiency of the polymer solar cells with silver nanowire electrodes is relatively low because they have transparent electrodes on both sides and thus exhibit low light absorption. These semitransparent devices, however, demonstrate the transparency of the wire mesh and also enable new applications, such as inexpensive window coatings that can generate power while reducing glare and providing aesthetically pleasing designs for buildings. The inset to Fig. 6a shows Hoover Tower on the Stanford University campus as viewed through the semitransparent solar cell measured in the main figure. Future work using our approach may allow applications, such as self-powered window displays or robust, touch-sensitive films that can wrap around prosthetic limbs, at very low cost.

In summary, we have demonstrated an optical method for welding together silver nanowires selectively at junction points by taking advantage of the extreme field concentration offered by plasmonics. The process is naturally self-limited owing to the very strong dependence of the plasmonic light concentration on the distance between the wires. Interestingly, this heating in the nanoscale junction is achieved on a length-scale many orders of magnitude smaller than the illumination spot size. As such, it allows new levels of control over heat generation and mass transport at the nanoscale that have not yet been demonstrated with laser annealing and are probably not even possible with furnace annealing. This opens up exciting new, simple and large-area processing schemes that facilitate rapid contacting of self-assembled, complex nanoscale devices and circuits or improved metal nanowire meshes. A direct application of our work is in the emerging solar cell, light-emitting diode and touch-screen display technologies, where the junction resistance between wires at present limits the performance[30,55]. A rapid and low-cost method for localized heating and welding only at the junction points could lead to significantly improved conduction properties without damaging heat-sensitive surrounding materials. We have demonstrated this principle by optically welding silver nanowire networks to make transparent electrodes on top of plastic wrap and heat-sensitive polymer solar cells, which is not possible with a standard heat treatment.

Methods

Silver nanowires were synthesized using the polyol process as previously reported. Briefly, 0.34 g of polyvinylpyrrolidone (PVP) was added to 20 ml of ethylene glycol and heated to 170 °C. Next, 25 mg of finely ground AgCl was added for the nucleation of silver seeds. After 3 min, 110 mg of $AgNO_3$ was added over the next 10 min and the mixture allowed to react for a further 30 min. The solution was cooled to room temperature and the nanowires were washed with methanol and precipitated by centrifugation at 6,000 rpm for 30 min. This was repeated three times to remove the ethylene glycol and excess PVP before redispersing the nanowires in 30 ml of methanol. The silver nanowires were dropcast onto silicon nitride windows suspended on silicon wafers with holes etched entirely through the backside using photolithographic patterning and KOH etching. The window size was approximately 250 μm × 250 μm × 30 nm. The thin silicon nitride allowed TEM imaging and electron diffraction before and after illumination. An FEI XL30 Sirion SEM and an FEI Tecnai G2 F20 X-TWIN TEM were used for all electron microscopy studies. The plasmonic nanowelding was performed using unpolarized, broadband illumination from 21 Ushio tungsten halogen lamps with a colour temperature of 3,050 K in an AG Heatpulse 210 system (Allwin21), at an illumination power density of approximately 30 W cm^{-2}. All nanowelding experiments were done in nitrogen ambient with 20 s.c.c.m. continuous purging. FEM simulations were performed using Comsol Multiphysics. Scattering spectra were collected using a Nikon Eclipse C1 confocal microscope coupled to a Princeton Instruments SpectraPro monochrometer and a photomultiplier tube detector. A halogen lamp and 50× objective were used for dark-field illumination and collection in reflection mode. The background-subtracted signal was normalized to the signal from a silver mirror to determine the scattering efficiency. Electron-beam lithography to electrically connect individual nanowires and junctions was performed on a JEOL SEM at 40 kV and with a beam current of 90 pA. Microchem PMMA A4 was used as the resist, spincoated at 4,000 rpm, exposed at a dose of 450 μC cm^{-2} and developed for 90 s in 1:3 methyl-isobutyl-ketone: isopropanol solution. Thermally evaporated Cr/Au (2 nm/100 nm) was used for the contact metal and liftoff was done in acetone for 3 h. All resistance measurements were performed on an Agilent semiconductor parameter analyser and total transmission measurements were taken with a home-built system composed of a Newport Tungsten–halogen source, monochromator, reference photodiodes and an integrating sphere. The silver nanowire mesh films used for transparent electrode measurements

versus illumination time were deposited on glass coverslips using a home-built spray-coating system to reduce sample-to-sample variations in performance. The contacts for four-point resistance measurements were Cr/Au films (2/100 nm) thermally evaporated through a shadow mask with 0.5 mm square holes equally spaced by 4 mm. The spray-coating system was also used to deposit silver nanowire films on Saran wrap and polymer solar cells, both of which were taped to a glass substrate. Polymer solar cells were produced on glass substrates patterned with an indium tin oxide transparent conductive electrode. Zinc oxide was deposited on top of the substrate by atomic layer deposition (approximately 15 nm) as an electron-selective contact for the subsequently deposited polymer–fullerene blend. Poly[N-9''-hepta-decanyl-2,7-carbazole-alt-5,5-(4′, 7′-di-2-thienyl-2′, 1′, 3′-benzothiadiazole)] (PCDTBT)/[6,6]-phenyl C70-butyric acid methyl ester ($PC_{70}BM$) (1:4 by weight) films were spincoated at 4,000 rpm for 1 min, leading to a final thickness of approximately 60 nm, as measured by profilometry. After drying at room temperature in a glove box for 24 h, the films were removed from the glove box and coated with a hole-conducting polymer from Plextronics (CA-1914) by spinning at 4,000 rpm for 1 min in air, followed by a 75 °C hotplate anneal in air for 15 min to remove residual solvent. Silver nanowires were spray-coated on top through a Kapton tape mask and the finished devices were measured before and after optical welding in nitrogen ambient. The standard hotplate treatment was 200 °C for 20 min in nitrogen. All solar cells were tested under 1 sun illumination using a Newport solar simulator. The power was adjusted to 1 sun by comparing the current to a reference silicon photodiode, using a KG-5 filter to account for the spectral mismatch.

Received 18 July 2011; accepted 3 January 2012; published online 5 February 2012

References

1. Baffou, G., Quidant, R. & Girard, C. Heat generation in plasmonic nanostructures: Influence of morphology. *Appl. Phys. Lett.* **94,** 153109 (2009).
2. Schuller, J. A. *et al.* Plasmonics for extreme light concentration and manipulation. *Nature Mater.* **9,** 193–204 (2010).
3. Hirsch, L. R. *et al.* Nanoshell-mediated near-infrared thermal therapy of tumors under magnetic resonance guidance. *Proc. Natl Acad. Sci. USA* **100,** 13549–13554 (2003).
4. Röntzsch, L., Heinig, K-H., Schuller, J. A. & Brongersma, M. L. Thin film patterning by surface-plasmon-induced thermocapillarity. *Appl. Phys. Lett.* **90,** 044105 (2007).
5. Govorov, A. O. *et al.* Gold nanoparticle ensembles as heaters and actuators: melting and collective plasmon resonances. *Nano. Res. Lett.* **1,** 84–90 (2006).
6. Soares, B., Jonsson, F. & Zheludev, N. All-optical phase-change memory in a single gallium nanoparticle. *Phys. Rev. Lett.* **98,** 153905 (2007).
7. Cao, L., Barsic, D. N., Guichard, A. R. & Brongersma, M. L. Plasmon-assisted local temperature control to pattern individual semiconductor nanowires and carbon nanotubes. *Nano Lett.* **7,** 3523–3527 (2007).
8. Boyd, D. A., Adleman, J. R., Goodwin, D. G. & Psaltis, D. Chemical separations by bubble-assisted interphase mass-transfer. *Anal. Chem.* **80,** 2452–2456 (2008).
9. Stehr, J. *et al.* Gold nanostoves for microsecond DNA melting analysis. *Nano Lett.* **8,** 619–623 (2008).
10. Halas, N. J., Lal, S., Chang, W-S., Link, S. & Nordlander, P. Plasmons in strongly coupled metallic nanostructures. *Chem. Rev.* **111,** 3913–3961 (2011).
11. Kneipp, K. *et al.* Single molecule detection using surface-enhanced Raman scattering (SERS). *Phys. Rev. Lett.* **78,** 1667–1670 (1997).
12. Brongersma, M. L., Hartman, J. W. & Atwater, H. A. Electromagnetic energy transfer and switching in nanoparticle chain arrays below the diffraction limit. *Phys. Rev. B* **62,** R16356–R16359 (2000).
13. Pendry, J. B., Schurig, D. & Smith, D. R. Controlling electromagnetic fields. *Science* **312,** 1780–1782 (2006).
14. Shalaev, V. M. Optical negative-index metamaterials. *Nature Photon.* **1,** 41–48 (2007).
15. Klein, M. W., Enkrich, C., Wegener, M. & Linden, S. Second-harmonic generation from magnetic metamaterials. *Science* **313,** 502–504 (2006).
16. Romero, I., Aizpurua, J., Bryant, G. W. & García de Abajo, F. J. Plasmons in nearly touching metallic nanoparticles: Singular response in the limit of touching dimers. *Opt. Express* **14,** 9988–9999 (2006).
17. García de Abajo, F. J. Nonlocal effects in the plasmons of strongly interacting nanoparticles, dimers, and waveguides. *J. Phys. Chem. C* **112,** 17983–17987 (2008).
18. Zuloaga, J., Prodan, E. & Nordlander, P. Quantum description of the plasmon resonances of a nanoparticle dimer. *Nano Lett.* **9,** 887–891 (2009).
19. Ward, D. R., Hüser, F., Pauly, F., Cuevas, J. C. & Natelson, D. Optical rectification and field enhancement in a plasmonic nanogap. *Nature Nanotech.* **5,** 732–736 (2010).
20. Gaynor, W., Burkhard, G. F., McGehee, M. D. & Peumans, P. Smooth nanowire/polymer composite transparent electrodes. *Adv. Mater.* **23,** 2905–2910 (2011).
21. Gaynor, W., Lee, J-Y. & Peumans, P. Fully solution-processed inverted polymer solar cells with laminated nanowire electrodes. *ACS Nano* **4,** 30–34 (2010).
22. Hecht, D. S., Hu, L. & Irvin, G. Emerging transparent electrodes based on thin films of carbon nanotubes, graphene, and metallic nanostructures. *Adv. Mater.* **23,** 1482–1513 (2011).
23. Kang, M-G., Xu, T., Park, H. J., Luo, X. & Guo, L. J. Efficiency enhancement of organic solar cells using transparent plasmonic Ag nanowire electrodes. *Adv. Mater.* **22,** 4378–4383 (2010).
24. Lee, J-Y., Connor, S. T., Cui, Y. & Peumans, P. Semitransparent organic photovoltaic cells with laminated top electrode. *Nano Lett.* **10,** 1276–1279 (2010).
25. Li, L. *et al.* Efficient flexible phosphorescent polymer light-emitting diodes based on silver nanowire–polymer composite electrode. *Adv. Mater.* **23,** 5563–5567 (2011).
26. Madaria, A. R., Kumar, A. & Zhou, C. Large scale, highly conductive and patterned transparent films of silver nanowires on arbitrary substrates and their application in touch screens. *Nanotechnology* **22,** 245201 (2011).
27. Yang, L. *et al.* Solution-processed flexible polymer solar cells with silver nanowire electrodes. *ACS Appl. Mater. Interf.* **3,** 4075–4084 (2011).
28. Yu, Z., Li, L., Zhang, Q., Hu, W. & Pei, Q. Silver nanowire–polymer composite electrodes for efficient polymer solar cells. *Adv. Mater.* **23,** 4453–4457 (2011).
29. Yu, Z. *et al.* Highly flexible silver nanowire electrodes for shape-memory polymer light-emitting diodes. *Adv. Mater.* **23,** 664–668 (2011).
30. Hu, L., Kim, H. S., Lee, J-Y., Peumans, P. & Cui, Y. Scalable coating and properties of transparent, flexible, silver nanowire electrodes. *ACS Nano* **4,** 2955–2963 (2010).
31. Karim, S. *et al.* Morphological evolution of Au nanowires controlled by Rayleigh instability. *Nanotechnology* **17,** 5954–5959 (2006).
32. Chen, H. *et al.* Transmission-electron-microscopy study on fivefold twinned silver nanorods. *J. Phys. Chem. B* **108,** 12038–12043 (2004).
33. Thompson, C. V. Grain growth in thin films. *Annu. Rev. Mater. Sci.* **20,** 245–268 (1990).
34. Lu, Y., Huang, J. Y., Wang, C., Sun, S. & Lou, J. Cold welding of ultrathin gold nanowires. *Nature Nanotech.* **5,** 218–224 (2010).
35. Guo, S. The creation of nanojunctions. *Nanoscale* **2,** 2521–2529 (2010).
36. Cui, Q., Gao, F., Mukherjee, S. & Gu, Z. Joining and interconnect formation of nanowires and carbon nanotubes for nanoelectronics and nanosystems. *Small* **5,** 1246–1257 (2009).
37. Kim, S. J. & Jang, D-J. Laser-induced nanowelding of gold nanoparticles. *Appl. Phys. Lett.* **86,** 033112 (2005).
38. Mafuné, F., Kohno, J-Y., Takeda, Y. & Kondow, T. Nanoscale soldering of metal nanoparticles for construction of higher-order structures. *J. Am. Chem. Soc.* **125,** 1686–1687 (2003).
39. Xu, S. *et al.* Nanometer-scale modification and welding of silicon and metallic nanowires with a high-intensity electron beam. *Small* **1,** 1221–1229 (2005).
40. Shin, H. *et al.* Photoresist-free lithographic patterning of solution-processed nanostructured metal thin films. *Adv. Mater.* **20,** 3457–3461 (2008).
41. Zhang, Y. *et al.* Tailoring the intrinsic metallic states of double-walled nanotube films by self-soldered laser welding. *Appl. Phys. Lett.* **91,** 233109 (2007).
42. Gu, Z., Ye, H., Bernfeld, A., Livi, K. J. T. & Gracias, D. H. Three-dimensional electrically interconnected nanowire networks formed by diffusion bonding. *Langmuir* **23,** 979–982 (2007).
43. Sommer, J. & Herzig, C. Direct determination of grain-boundary and dislocation self-diffusion coefficients in silver from experiments in type-C kinetics. *J. Appl. Phys.* **72,** 2758–2766 (1992).
44. Prokes, S. M., Alexson, D., Glembocki, O. J., Park, H. D. & Rendell, R. W. Plasmonic behavior of Ag/dielectric nanowires and the effect of geometry. *J. Vacuum Sci. Technol. B* **27,** 2055–2061 (2009).
45. Holland, W. & Hall, D. Frequency shifts of an electric-dipole resonance near a conducting surface. *Phys. Rev. Lett.* **52,** 1041–1044 (1984).
46. Hu, M., Ghoshal, A., Marquez, M. & Kik, P. G. Single particle spectroscopy study of metal-film-induced tuning of silver nanoparticle plasmon resonances. *J. Phys. Chem. C* **114,** 7509–7514 (2010).
47. Mock, J. J. *et al.* Distance-dependent plasmon resonant coupling between a gold nanoparticle and gold film. *Nano Lett.* **8,** 2245–2252 (2008).
48. Chu, Y. & Crozier, K. B. Experimental study of the interaction between localized and propagating surface plasmons. *Opt. Lett.* **34,** 244–246 (2009).
49. Knight, M. W. *et al.* Nanoparticle-mediated coupling of light into a nanowire. *Nano Lett.* **7,** 2346–2350 (2007).
50. Hao, F. & Nordlander, P. Plasmonic coupling between a metallic nanosphere and a thin metallic wire. *Appl. Phys. Lett.* **89,** 103101 (2006).
51. Wei, H. *et al.* Polarization dependence of surface-enhanced Raman scattering in gold nanoparticle–nanowire systems. *Nano Lett.* **8,** 2497–2502 (2008).
52. Le, F. *et al.* Plasmons in the metallic nanoparticle–film system as a tunable impurity problem. *Nano Lett.* **5,** 2009–2013 (2005).

53. Cao, L., Fan, P., Barnard, E. S., Brown, A. M. & Brongersma, M. L. Tuning the color of silicon nanostructures. *Nano Lett.* 2649–2654 (2010).
54. Du, C. *et al*. Confocal white light reflection imaging for characterization of metal nanostructures. *Opt. Commun.* **281,** 5360–5363 (2008).
55. Lee, J-Y., Connor, S. T., Cui, Y. & Peumans, P. Solution-processed metal nanowire mesh transparent electrodes. *Nano Lett.* **8,** 689–692 (2008).

Acknowledgements

This publication was based on work supported by the Center for Advanced Molecular Photovoltaics (CAMP) (Award No KUS-C1-015-21), funded by King Abdullah University of Science and Technology (KAUST). Y.C. acknowledges support from KAUST Investigator Award (No. KUS-I1-001-12). We gratefully acknowledge valuable discussions with P. Nordlander on the optical coupling of metallic nanostructures. E.C.G. acknowledges partial support from the Global Climate and Energy Project at Stanford University.

Author contributions

E.C.G. and M.L.B. conceived of the experiments, W.C. performed the FEM simulations, J.J.C. performed the TEM, S.T.C. synthesized the silver nanowires, F.M. assisted with the dark-field scattering measurements, M.G.C. built the spray-coating set-up and deposited the silver nanowires on the polymer solar cells and Saran wrap, and E.C.G. performed all other experiments. M.L.B., Y.C. and M.D.M. supervised the project. E.C.G. and M.L.B. wrote the manuscript. All authors discussed the results and contributed to the final version of the manuscript.

Additional information

The authors declare no competing financial interests. Supplementary information accompanies this paper on www.nature.com/naturematerials. Reprints and permissions information is available online at http://www.nature.com/reprints. Correspondence and requests for materials should be addressed to M.L.B.